DUAL-ANTENNA PASSIVE SYNTHETIC APERTURE DOA ESTIMATION FOR AIRBORNE PLATFORMS

Leandro Geraldo da Costa, Daniele Oliveira Silva, Romildo Henrique de Souza, and Felix Antreich

***Abstract*— This work presents a dual-antenna passive synthetic aperture Direction-of-Arrival (DoA) estimation approach for compact airborne sensors. A physics-based model is employed, incorporating spherical wave propagation, Doppler effects, and a 200 km Line-of-Sight (LOS), which is implemented in an in-house radar simulator. The corresponding Cramer-Rao Lower Bound (CRLB) is derived to analyze the estimator's behavior and, in particular, to explore the trade-off between aperture length Q and number of snapshots K. Computer simulations conducted over a 0–50 dB Signal-to-Noise Ratio (SNR) range demonstrate high azimuth and elevation accuracy, convergence of the Root Mean Square (RMS) error to the theoretical lower bound, and robustness. The proposed scheme offers a low size, weight, and power (SWaP) solution for passive airborne sensing platforms.**

***Keywords*— Passive radar, synthetic aperture, antenna arrays, direction-of-arrival, airborne platforms, Cramer–Rao lower bound**

I. INTRODUCTION

High-resolution Direction-of-Arrival (DoA) estimation is crucial in surveillance, navigation, and electronic warfare for detecting and localizing radio sources [1]. While classical multi-antenna arrays are effective, their bulky and power-hungry front-ends make them unsuitable for low size, weight, and power (SWaP) platforms like small aircraft or drones [2].

To overcome these limitations, passive synthetic aperture methods have emerged, leveraging platform motion to emulate a large virtual array with minimal hardware. Foundational work by Cheng et al. [3] demonstrated that a single moving receiver, combined with high-resolution algorithms like MUSIC, could achieve accurate DoA estimates using simple and low-cost hardware. Building on this, other researchers have focused on enhancing single-sensor synthetic aperture positioning by developing robust signal processing to compensate for motion-induced phase variations and enable coherent data accumulation, significantly improving performance in low Signal-to-Noise Ratio (SNR) environments [4].

However, these single-sensor synthetic aperture systems are fundamentally limited to estimating the azimuth angle [5] and suffer from ambiguities over a wide Field-of-View (FoV). While adding a second sensor to form a simple interferometer is a well-known solution for resolving elevation, the state-of-the-art lacks a comprehensive analysis of such a dual-antenna configuration within a synthetic aperture framework under realistic airborne conditions. Specifically, few estimators are designed to handle the combined challenges of spherical wave propagation, Doppler effects from airborne platforms, and the need to maintain accuracy over long-range Line-of-Sight (LoS) links. This work addresses that gap.

In this work, we present and analyze a dual-antenna passive synthetic-aperture DoA estimation approach tailored to such challenging scenarios. We develop a physics-based signal model incorporating spherical wave propagation and Doppler effects over a 200 km LoS. This model is implemented in the *Advanced Radar Simulator (ARS)*, an in-house software developed at the Aeronautics Institute of Technology (ITA) [6]. The corresponding Cramer-Rao Lower Bound (CRLB)[1] is derived to analyze the estimator's behavior and guide the trade-off between synthetic aperture length (Q) and the number of snapshots (K)[2].

Comprehensive simulations confirm that, for practical aperture–snapshot combinations such as $Q = 500$ and $K = 2$, the proposed architecture maintains low Root Mean Square (RMS) DoA error across the entire 0–50 dB SNR range. These results demonstrate the feasibility and robustness of dual-antenna passive synthetic apertures for low-SWaP airborne platforms and provide a solid foundation for future work on multi-source scenarios and intra-pulse modulation exploitation.

II. SENSING SCENARIO

In order to evaluate the proposed dual-antenna synthetic-aperture system, we consider a representative airborne sensing scenario. This scenario is characterized by the LoS range between the airborne platform and a stationary ground emitter, as well as their relative altitude. The receiver is equipped with two antennas, spaced by $\lambda/2$, enabling phase-coherent signal reception. The platform flies eastwards at a constant speed of $v = 200\,\text{m/s}$; the antennas, arranged in a vertical Uniform Linear Array (ULA), remain oriented toward the radio source. This motion generates a wide virtual aperture in the azimuth direction and provides an instantaneous interferometric baseline in elevation. The emitter is localized by

Leandro Geraldo da Costa, Daniele Oliveira Silva, Romildo Henrique de Souza, and Felix Antreich, Department of Telecommunications, Aeronautics Institute of Technology (ITA), São José dos Campos - São Paulo, e-mail: leandrocosta2008@gmail.com, daniele19954@gmail.com, romildohsouza@gmail.com, fean@ita.br; This work was partially supported by the Brazilian National Council for Scientific and Technological Development (CNPq) under grant 312394/2021-7 PQ-2, 406517/2022-3, 407245/2022-7, and 313901/2025-2, and by Brazil´s Funding Authority for Studies and Projects (FINEP) under grant 01.22.0581.00.

[1]The CRLB sets the minimum achievable error variance for any unbiased estimator; an estimator that attains this bound is called efficient [7], [8].

[2]Following the common use in array processing literature [2], the word *snapshot* denotes any measurement vector that is processed coherently.

performing DoA estimation at successive positions along the same flight heading. We assume that the platform's position and attitude are known precisely.

We consider a 200 km LoS link at near-zero elevation. Since the airborne receiver and ground emitter are almost coplanar, the vertical geometry is unfavorable, making the dual-antenna baseline essential for accurate elevation estimation. All signal and flight dynamics are generated with the *ARS*, it recreates the complete sensing scenario. A summary of the key geometry, platform, and waveform parameters is given in Table I and the virtual arrays and snapshot combinations used in this work with the synthetic aperture (in millimeters) for each pair (K, Q) are shown in Table II.

TABLE I: Scenario parameters.

Geometry & Operating		**Transmit & Signal**	
Par.	**Val.**	**Par.**	**Val.**
LoS [km]	200	f_c [GHz]	26
Sens. alt. [m]	0	PW [ns]	10 000
El. [°]	0	PRP [kHz]	10
Vel. [m/s]	200	Ant. pat. (Radar)	Omni
Fs [MHz]	200	Doppler	Yes
Ant. pat. (Sensor)	Omni	Freq. off. mod.	No
$\lvert f_d \rvert_{\max}$ [kHz]	~ 17.35	Prop. mod.	Spherical
Radar alt. [m]	0	Sig. type	Rect. pulse

TABLE II: S. Aper. length for the selected (Q, K) pairs.

Q	2	10	20	50	100	500	500	1000
K	1000	200	100	40	20	4	2	2
S. Aper. (mm)	0.001	0.009	0.019	0.049	0.099	0.499	0.499	0.999

III. Signal Model

Under the far-field assumption, the signal is assumed to reach the center of the ULA (at position $\mathbf{p}_n$) in discrete time intervals of $(n-1)T_s$, where T_s is the sampling duration and $n = 1, 2, 3, \ldots$. We consider a synthetic aperture along the x-axis with a size of Q consecutive samples. The unit vector

$$\mathbf{u}^{\mathsf{T}} = \left[\, \sin(\theta)\cos(\varphi) \;\; \sin(\theta)\sin(\varphi) \;\; \cos(\theta) \,\right] = \left[\, u_x \;\; u_y \;\; u_z \,\right], \tag{1}$$

oriented perpendicular to the incident planar wavefront, indicates the DoA relative to the antenna coordinate system's center, which moves with the platform for each snapshot $k = 1, \ldots, K$, as shown in Fig. 1. In this synthetic aperture setup with two physical antenna elements, the azimuth angle φ, which is part of the DoA, is measured from the x-axis toward the y-axis, intersecting the projection of $\mathbf{u}$ onto the xy-plane. The elevation angle θ is measured from the z-axis toward $\mathbf{u}$.

We assume the two antennas are separated by a distance $\delta = \lambda/2$, placing them at fixed z-coordinates of $z = \pm\delta/2$. While these antennas are fixed in the vertical dimension, the array (or platform) traverses discrete sampling points along the x-axis with an inter-sampling distance of $\Delta = v_x T_s$, where v_x is the velocity of the platform. The antenna positions in each of the K consecutive blocks, each with its own coordinate system, are denoted by a single expression:

$$\mathbf{d}_{i,k,l} = \left[\left(\tfrac{Q+1}{2} - l\right)\Delta \quad 0 \quad \tfrac{\delta}{2}(-1)^{i+1}\right]^{\mathsf{T}}, \quad i \in \{1, 2\}. \tag{2}$$

Here, the index l denotes the local sample number within a specific block k, where l ranges from 1 to Q. This local index is derived from the absolute sample index n using the relation $l = n - Q(k-1)$. The index i, in turn, distinguishes between the two antennas. This format concisely represents the common x-coordinate and the opposing z-coordinates for each antenna pair.

Thus, the time delay at sensor $\mathbf{d}_{i,k,l} = [d_{i,k,l,x} \;\; d_{i,k,l,y} \;\; d_{i,k,l,z}]^{\mathsf{T}}$ is given by

$$\tau_{i,k,l} = \frac{1}{c}\,\mathbf{u}^{\mathsf{T}}\mathbf{d}_{i,k,l} = \frac{1}{c}\left(\left(\frac{Q+1}{2} - l\right)\Delta\,\sin(\theta)\cos(\varphi) + \frac{\delta}{2}(-1)^{i+1}\,\cos(\theta)\right), \tag{3}$$

where c is the speed of light.

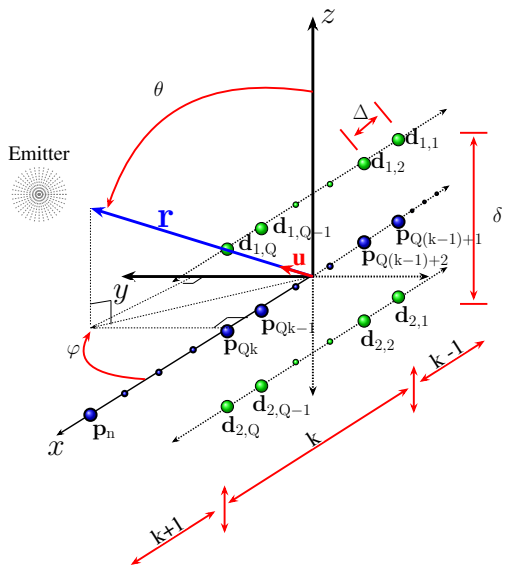

Fig. 1: Synthetic aperture for Q samples and K snapshots.

Let $s(t) \in \mathbb{C}$ be a signal impinging on the ULA from $\mathbf{u}$. The complex baseband signal at $\mathbf{d}_{i,k,l}$ is

$$\underbrace{\begin{bmatrix} y_{1,k}((l-1)T_s) \\ y_{2,k}((l-1)T_s) \end{bmatrix}}_{=\mathbf{x}_k[l]} = \begin{bmatrix} s_k\big((l-1)T_s - \tau_{1,k,l}\big)\, e^{-j2\pi f_c \tau_{1,k,l}} \\ s_k\big((l-1)T_s - \tau_{2,k,l}\big)\, e^{-j2\pi f_c \tau_{2,k,l}} \end{bmatrix} + \underbrace{\begin{bmatrix} \mathrm{n}_{1,k}((l-1)T_s) \\ \mathrm{n}_{2,k}((l-1)T_s) \end{bmatrix}}_{=\mathbf{n}_k[l]} \tag{4}$$

where $\mathbf{n}_k[l]$ is additive complex white Gaussian noise with $\mathcal{CN}(0, \sigma_n^2)$. Assuming the signal $s(t)$ is narrowband, for Q consecutive time instances, the difference between consecutive delays can be approximated as

$$\tau_{i,k,(l+2)} - \tau_{i,k,(l+1)} \approx \tau_{i,k,(l+3)} - \tau_{i,k,(l+2)} \approx \cdots \approx \tau_{i,k,Q} - \tau_{i,k,Q-1}. \tag{5}$$

Furthermore, we assume that for Q consecutive samples, also the complex envelope $s_k((l-1)T_s) = s_k[l]$, for $l = 1, 2, \ldots, Q$ can be approximated as

$$s_k[1] \approx s_k[2] \approx s_k[3] \approx \cdots \approx s_k[Q]. \tag{6}$$

Thus, we can write

$$\mathbf{x}_k[l] \approx s_k[l] \begin{bmatrix} e^{-j2\pi f_c \tau_{1,k,l}} \\ e^{-j2\pi f_c \tau_{2,k,l}} \end{bmatrix} + \mathbf{n}_k[l]. \tag{7}$$

Finally, we can rearrange the phase term of the received signal as a left centro-hermitian steering vector $\mathbf{a}(\varphi, \theta, f_c, v_x, T_s)$ for each snapshot k and write the received signal in vector notation. In the expression below, we use $s_k[Q]$, the envelope of the last sample within each block, as the representative value for the stationary signal envelope.

$$\begin{aligned}
\mathbf{y}[k] \triangleq & \underbrace{e^{-j\,\frac{2\pi}{\lambda}\,(k-1)\,Q\,\Delta\,\sin(\theta)\cos(\varphi)} s_k[Q]}_{=\tilde{s}[k]} \\
& \underbrace{\begin{bmatrix}
e^{+j\,\frac{2\pi\Delta}{\lambda}\left(\frac{Q-1}{2}\,\sin(\theta)\cos(\varphi) + \frac{\delta}{2\Delta}\,\cos(\theta)\right)} \\
e^{+j\,\frac{2\pi\Delta}{\lambda}\left(\frac{Q-1}{2}\,\sin(\theta)\cos(\varphi) - \frac{\delta}{2\Delta}\,\cos(\theta)\right)} \\
e^{+j\,\frac{2\pi\Delta}{\lambda}\left(\frac{Q-3}{2}\,\sin(\theta)\cos(\varphi) + \frac{\delta}{2\Delta}\,\cos(\theta)\right)} \\
e^{+j\,\frac{2\pi\Delta}{\lambda}\left(\frac{Q-3}{2}\,\sin(\theta)\cos(\varphi) - \frac{\delta}{2\Delta}\,\cos(\theta)\right)} \\
\vdots \\
e^{-j\,\frac{2\pi\Delta}{\lambda}\left(\frac{Q-3}{2}\,\sin(\theta)\cos(\varphi) - \frac{\delta}{2\Delta}\,\cos(\theta)\right)} \\
e^{-j\,\frac{2\pi\Delta}{\lambda}\left(\frac{Q-3}{2}\,\sin(\theta)\cos(\varphi) + \frac{\delta}{2\Delta}\,\cos(\theta)\right)} \\
e^{-j\,\frac{2\pi\Delta}{\lambda}\left(\frac{Q-1}{2}\,\sin(\theta)\cos(\varphi) - \frac{\delta}{2\Delta}\,\cos(\theta)\right)} \\
e^{-j\,\frac{2\pi\Delta}{\lambda}\left(\frac{Q-1}{2}\,\sin(\theta)\cos(\varphi) + \frac{\delta}{2\Delta}\,\cos(\theta)\right)}
\end{bmatrix}}_{=\mathbf{a}(\varphi,\theta,f_c,v_x,T_s)} + \underbrace{\begin{bmatrix} \mathbf{n}_k[1] \\ \mathbf{n}_k[2] \\ \vdots \\ \mathbf{n}_k[Q] \end{bmatrix}}_{=\tilde{\mathbf{n}}[k]} \\
= & \ \mathbf{a}\big(\varphi, \theta, f_c, v_x, T_s\big)\, \tilde{s}[k] \ + \ \tilde{\mathbf{n}}[k].
\end{aligned} \tag{8}$$

Assuming that the angles of arrival φ and θ are constant for K snapshots we can write a signal model in matrix form collecting K snapshots

$$\mathbf{Y} = \ \mathbf{a}(\varphi, \theta, f_c, v_x, T_s)\, \tilde{\mathbf{s}}^{\mathrm{T}} \ + \ \mathbf{N} \ \in \ \mathbb{C}^{2Q \times K}, \tag{9}$$

where

$$\mathbf{Y} = \left[\, \mathbf{y}[1] \ \mathbf{y}[2] \ \ldots \ \mathbf{y}[K] \,\right], \tag{10}$$

$$\mathbf{N} = \left[\, \tilde{\mathbf{n}}[1] \ \tilde{\mathbf{n}}[2] \ \ldots \ \tilde{\mathbf{n}}[K] \,\right], \tag{11}$$

$$\tilde{\mathbf{s}} = \left[\tilde{s}[1], \tilde{s}[2], \ldots, \tilde{s}[K]\right]^{\mathrm{T}}. \tag{12}$$

Multiplying $s_k[Q]$ by $e^{-j\,\frac{2\pi}{\lambda}\,(k-1)\,Q\,\Delta\,\sin(\theta)\cos(\varphi)}$ implements a global phase shift applied to each snapshot k that compensates for the platform displacement. Hence, the center of the synthetic aperture coordinate system for each snapshot k always coincides with the center of the first snapshot ($k = 1$).

IV. DoA Estimation

In this work, we apply the Maximum Likelihood Estimator (MLE) to estimate the DoA, which for a single impinging wavefront is equivalent to the so-called conventional beamformer applied to DoA estimation [8].

The spatial covariance matrix $\mathbf{R}_{\mathbf{yy}}$ can be estimated based on $2Q \times K$ snapshots

$$\hat{\mathbf{R}}_{\mathbf{yy}} = \frac{1}{K} \sum_{k=1}^{K} \mathbf{y}[k]\mathbf{y}^{\mathrm{H}}[k] = \frac{1}{K} \mathbf{Y}\mathbf{Y}^{\mathrm{H}} \in \mathbb{C}^{2Q \times 2Q}. \tag{13}$$

The MLE for the DoA, azimuth and elevation angles, in the single-source case can be given as

$$(\hat{\varphi}, \hat{\theta}) = \underset{\varphi,\theta}{\arg\max} \left\{ \mathbf{a}^{\mathrm{H}}(\varphi, \theta, f_c, v_x, T_s)\, \hat{\mathbf{R}}_{\mathbf{yy}}\, \mathbf{a}(\varphi, \theta, f_c, v_x, T_s) \right\}. \tag{14}$$

To solve for $(\hat{\varphi}, \hat{\theta})$, a two-dimensional grid search is used to roughly estimate the maximum of the likelihood function and the Nelder-Mead optimization method [9] is applied for refinement.

First, an initial coarse grid search is performed for φ ranging from 0° to 180° and for θ ranging from 90° to 120°, using a resolution of 1° in both cases. These initial coarse searches provide estimates of angles, which are subsequently refined using the Nelder–Mead method, with a tolerance of 10^{-2} for angle parameters and 10^{-14} for the cost function, restricted to a maximum iteration limit of 500. In addition to that, a penalty function terminates the optimization if the angle variation exceeds 5°.

V. Cramer–Rao Lower Bound (CRLB)

We now derive the CRLB for the estimation of the DoA for the dual-antenna synthetic aperture data model defined in (8) and (9). We consider that the Doppler effect and spherical-wave propagation effects are negligible for the sensing scenario. Recall that each of the Q aperture positions has two physical antenna elements, yielding $2Q$ total measurements per snapshot k, and we collect K snapshots.

To derive the CRLB, it is convenient to vectorize $\mathbf{Y}$ as $\tilde{\tilde{\mathbf{y}}} = \mathrm{vec}(\mathbf{Y}) \in \mathbb{C}^{2QK \times 1}$. Then

$$\tilde{\tilde{\mathbf{y}}} = \tilde{\mathbf{s}} \otimes \mathbf{a}(\varphi, \theta, f_c, v_x, T_s) \ + \ \tilde{\tilde{\mathbf{n}}}, \tag{15}$$

where $\tilde{\tilde{\mathbf{n}}} = \mathrm{vec}(\mathbf{N}) \sim \mathcal{CN}\big(\mathbf{0}, \sigma^2 \mathbf{I}_{2QK}\big)$ and $\otimes$ denotes the Kronecker product. Defining

$$\boldsymbol{\mu}(\varphi, \theta) = \tilde{\mathbf{s}} \otimes \mathbf{a}(\varphi, \theta, f_c, v_x, T_s), \tag{16}$$

the Fisher Information Matrix (FIM) for the parameter vector $\boldsymbol{\eta} = [\,\varphi,\ \theta\,]^{\mathrm{T}}$ for the complex multivariate Gaussian case can be given by [7]

$$\mathbf{F}(\boldsymbol{\eta}) = \tfrac{2}{\sigma^2}\, \mathrm{Re}\left\{ \begin{bmatrix} \left\| \frac{\partial \boldsymbol{\mu}(\varphi,\theta)}{\partial \varphi} \right\|_2^2 & \left(\frac{\partial \boldsymbol{\mu}(\varphi,\theta)}{\partial \varphi} \right)^{\mathrm{H}} \frac{\partial \boldsymbol{\mu}(\varphi,\theta)}{\partial \theta} \\ \left(\frac{\partial \boldsymbol{\mu}(\varphi,\theta)}{\partial \theta} \right)^{\mathrm{H}} \frac{\partial \boldsymbol{\mu}(\varphi,\theta)}{\partial \varphi} & \left\| \frac{\partial \boldsymbol{\mu}(\varphi,\theta)}{\partial \theta} \right\|_2^2 \end{bmatrix} \right\}. \tag{17}$$

Further reformulating[3] (17) we get

$$\mathbf{F}(\boldsymbol{\eta}) = \frac{2\,\|\tilde{\mathbf{s}}\|^2}{\sigma^2}\, \mathrm{Re}\{\mathbf{J}\} = \frac{2\,\|\tilde{\mathbf{s}}\|^2}{\sigma^2} \mathrm{Re}\left\{ \begin{bmatrix} J_{1,1} & J_{1,2} \\ J_{2,1} & J_{2,2} \end{bmatrix} \right\} \tag{18}$$

[3] $(\mathbf{a} \otimes \mathbf{b})^{\mathrm{H}}(\mathbf{a} \otimes \mathbf{c}) = \mathbf{a}^{\mathrm{H}}\mathbf{a} \otimes \mathbf{b}^{\mathrm{H}}\mathbf{c} = ||\mathbf{a}||_2^2 \otimes \mathbf{b}^{\mathrm{H}}\mathbf{c} = ||\mathbf{a}||_2^2 \mathbf{b}^{\mathrm{H}}\mathbf{c}$ with $\mathbf{a} \in \mathbb{C}^N$,$\mathbf{b} \in \mathbb{C}^N$, and $\mathbf{c} \in \mathbb{C}^N$.

with

$$J_{1,1} = \left\| \frac{\partial \mathbf{a}(\varphi,\theta,f_c,v_x,T_s)}{\partial \varphi} \right\|_2^2 \tag{19}$$

$$J_{1,2} = \left(\frac{\partial \mathbf{a}(\varphi,\theta,f_c,v_x,T_s)}{\partial \varphi} \right)^{\mathrm{H}} \frac{\partial \mathbf{a}(\varphi,\theta,f_c,v_x,T_s)}{\partial \theta} \tag{20}$$

$$J_{2,1} = \left(\frac{\partial \mathbf{a}(\varphi,\theta,f_c,v_x,T_s)}{\partial \theta} \right)^{\mathrm{H}} \frac{\partial \mathbf{a}(\varphi,\theta,f_c,v_x,T_s)}{\partial \varphi} \tag{21}$$

$$J_{2,2} = \left\| \frac{\partial \mathbf{a}(\varphi,\theta,f_c,v_x,T_s)}{\partial \theta} \right\|_2^2. \tag{22}$$

The

For clarity in the plots, we re-center both angles around the virtual antenna boresight as follows:

$$\varphi_{\text{ant}} = \varphi - 90^\circ, \quad \theta_{\text{ant}} = 90^\circ - \theta. \tag{23}$$

Figure 2 shows the RMS azimuth error for various combinations of Q and K at $\mathrm{SNR} = 0\,\mathrm{dB}$. The following observations can be made:

- **Azimuth-dependent degradation:** For short apertures, such as $Q = 2$, MLE convergence failures produce outliers at the FoV limit. The estimation algorithm defaults to $\varphi_{\text{ant}} = 0^\circ$ to manage these cases, creating an RMS error "ramp" as this incorrect angle persists across the azimuth range.
- **Sample-budget trade-off:** For a fixed 2000-sample budget, a longer synthetic aperture (Q) is more effective than more snapshots (K).
- **Virtual aperture size:** With larger Q, the error profile flattens from a "ramp" to a "plateau" within the 0°–60° azimuth range, indicating more stable performance, especially for $Q \geq 100$.

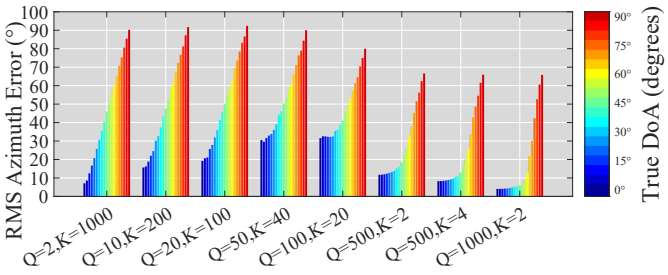

Fig. 2: RMS azimuth error vs. Q, K values. $\mathrm{SNR} = 0$ dB.

To highlight the "plateau" behaviour, Fig. 3 plots the CRLB for the signal model as a function of SNR for several (Q, K) pairs at a fixed boresight azimuth $\varphi_{\text{ant}} = 0^\circ$ and $\theta_{\text{ant}} = 0^\circ$. As expected, for a restricted number of samples, enlarging the synthetic aperture (Q) lowers the bound.

Fig. 4 keeps $Q = 500$ and $K = 2$ constant and shows the CRLB (Signal Model) vs. SNR for a set of azimuth angles φ_{ant}. One can see that for larger φ_{ant} the CRLB tends to infinity, suggesting an identifiable problem for larger φ_{ant}, as can be observed in Table III for φ_{ant} = 89.99°.

Detailed insight into the outlier behavior of the MLE is provided in Fig. 5 for $Q = 500$ and $K = 2$. When φ_{ant} is in the range from -90° to $+90^\circ$, the MLE exhibits heavier tails, especially at lower SNR and still a large number of outliers at moderate to higher. Restricting φ_{ant} to a range of $\pm 60^\circ$, as shown in Fig. 6, significantly reduces outliers and improves overall robustness.

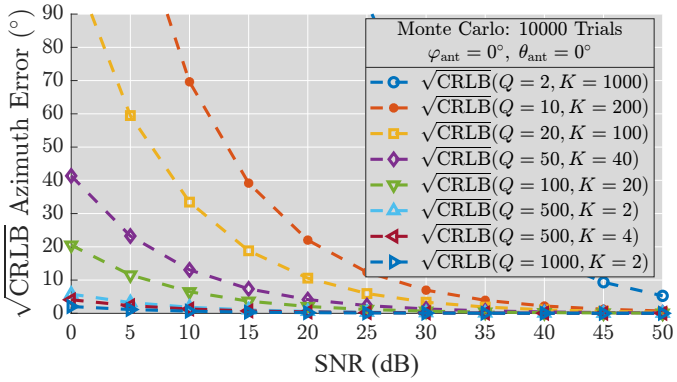

Fig. 3: $\sqrt{\text{CRLB}}$ vs. SNR for combinations of Q and K.

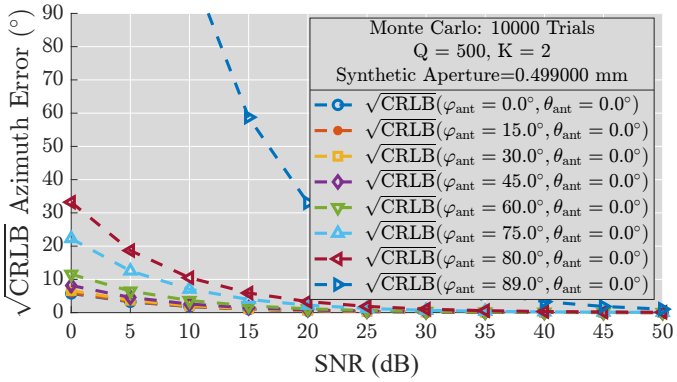

Fig. 4: $\sqrt{\text{CRLB}}$ vs. SNR for different φ_{ant} and $\theta_{\text{ant}} = 0^\circ$.

TABLE III: $\sqrt{\text{CRLB}}$ at $\varphi_{\text{ant}} = 89.99^\circ$, $\theta_{\text{ant}} = 0^\circ$ versus SNR.

SNR (dB)	0	5	10	15
$\sqrt{\text{CRLB}}_{\varphi_{\text{ant}}=89.99^\circ}$ (°)	3.30×10^4	1.86×10^4	1.05×10^4	5.88×10^3
SNR (dB)	20	25	30	35
$\sqrt{\text{CRLB}}_{\varphi_{\text{ant}}=89.99^\circ}$ (°)	3.30×10^3	1.86×10^3	1.05×10^3	5.88×10^2
SNR (dB)	40	45	50	
$\sqrt{\text{CRLB}}_{\varphi_{\text{ant}}=89.99^\circ}$ (°)	3.30×10^2	1.86×10^2	1.05×10^2	

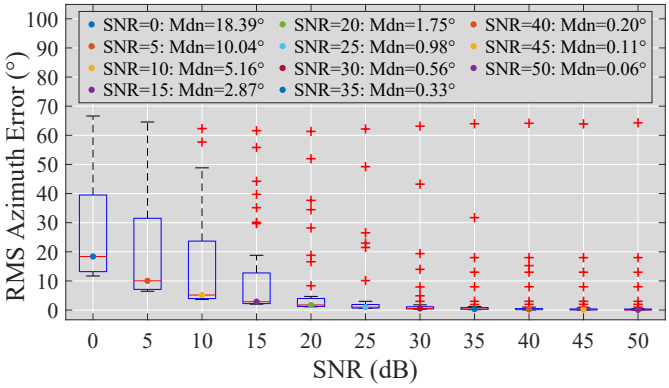

Fig. 5: Boxplot for $Q = 500, K = 2$. $\varphi_{\text{ant}} \in [-90^\circ, +90^\circ]$.

Fig. 7 compares the RMS azimuth error to the $\sqrt{\text{CRLB}}$ for $Q = 500$ and $K = 2$. For $\mathrm{SNR} \gtrsim 25\,\mathrm{dB}$, both simulation results closely match the theoretical bound, demonstrating that the MLE is efficient at moderate to higher SNR. Thus, the Doppler effect and spherical-wave propagation are negligible in this simulated scenario. In contrast, the estimation of $\hat{\theta}_{\text{ant}}$

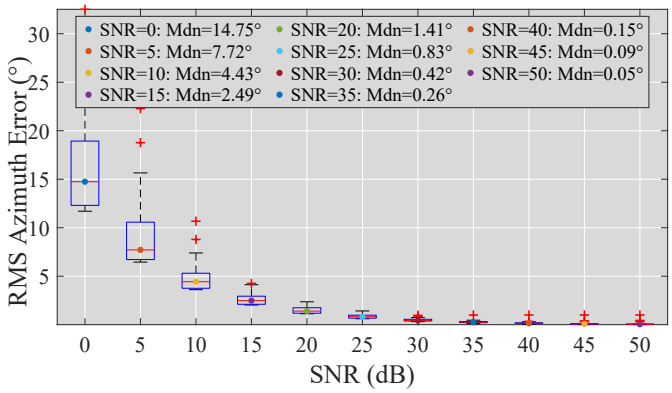

Fig. 6: Boxplot for $Q = 500, K = 2$. $\varphi_{\text{ant}} \in [-60°, +60°]$.

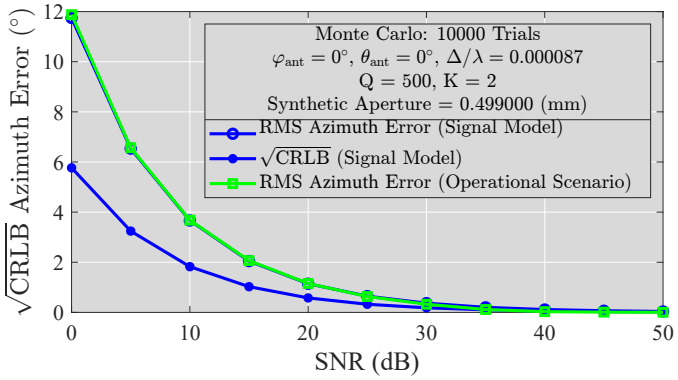

Fig. 7: RMS azimuth error and $\sqrt{\text{CRLB}}$ vs. SNR.

benefits substantially from the half-wavelength spacing between the two physical antennas. This fixed baseline provides direct elevation discrimination that does not depend strongly on the virtual aperture size. Fig. 8 shows the RMS error of $\hat{\theta}_{\text{ant}}$ across positive azimuth angles at $\text{SNR} = 0\,\text{dB}$. The results show relatively stable performance for all (Q, K) set, without convergence problems in the complete FoV.

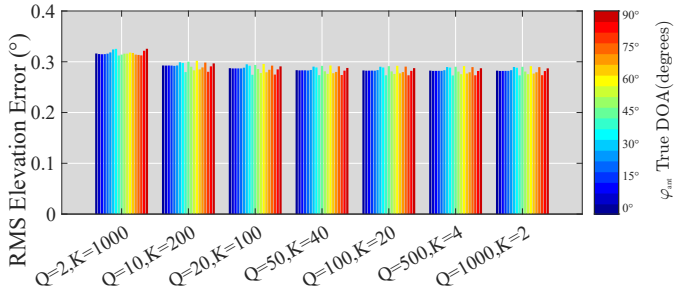

Fig. 8: RMS elevation error vs. Q, K values. $\text{SNR} = 0$ dB.

As expected, Fig. 9 shows that CRLB for the elevation angles maintains the same behavior throughout the azimuth angle range of φ_{ant}.

VI. Conclusion

In this work we investigated a dual-antenna synthetic aperture DoA estimation approach for airborne platforms using

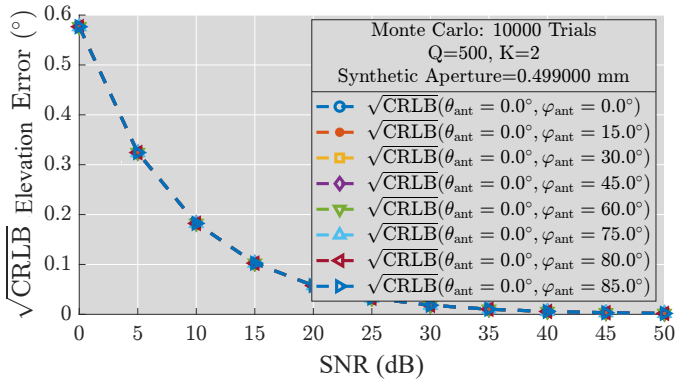

Fig. 9: $\sqrt{\text{CRLB}}$ for elevation angle θ_{ant} and different φ_{ant}.

the ARS. The derived CRLB for the case that Doppler effect and spherical-wave propagation are negligible showed that two closely spaced elements can achieve sub-degree azimuth–elevation accuracy over a broad SNR range. Key takeaways are:

1) Longer synthetic apertures boost azimuth resolution.
2) As Q increases, performance within the 120° FoV noticeably outperforms that at other angles.
3) The MLE approaches the CRLB in moderate to high SNR for φ_{ant} and can be considered efficient for θ_{ant}.

This compact approach suits airborne passive sensing under strict SWaP constraints. Future work may include multi-source scenarios, advanced pulse modulation, and robustness to frequency offsets and clutter in more complex environments.

References

[1] S. CHANDRAN, *Advances in Direction-of-Arrival Estimation*. Norwood, MA: Artech House, 2005. [Online]. Available: https://ieeexplore.ieee.org/document/9100030

[2] H. L. VAN TREES, *Optimum Array Processing. Detection, Estimation and Modulation Theory, Part IV*. New York, NY: Wiley Interscience, 2002.

[3] K. Q. F. CHENG, J.; GUAN, "Direction-of-arrival estimation with virtual antenna array: Observability analysis, local oscillator frequency offset compensation, and experimental results," *IEEE Transactions on Instrumentation and Measurement*, vol. 70, pp. 1–13, 2021.

[4] G.-C. W. Y. Z. Z. X. M. Y. X. WANG, Y.; SUN, "A high-resolution and high-precision passive positioning system based on synthetic aperture technique," *IEEE Transactions on Geoscience and Remote Sensing*, vol. 60, pp. 1–13, 2022.

[5] D. O. A. F. D. DA COSTA, L. G.; SILVA, "Single antenna passive synthetic aperture doa estimation," in *Proceedings of the Symposium on Operational Applications in Defense Areas*. São José dos Campos: Instituto Tecnológico de Aeronáutica, 2024.

[6] I. T. D. AERONÁUTICA, "Simulador avançado de radar: programa de computador," Rio de Janeiro, 2024, certificado de Registro de Programa de Computador, Processo BR512025001025-7. Publicado em 22 mar. 2024. Expedido em 25 mar. 2025.

[7] S. M. KAY, *Fundamentals of Statistical Signal Processing: Estimation Theory*. Englewood Cliffs, NJ: Prentice-Hall, 1993.

[8] N. O'DONOUGHUE, *Emitter Detection and Geolocation for Electronic Warfare*, ser. Artech House electronic warfare library. Boston, MA: Artech House, 2019. [Online]. Available: https://books.google.com.br/books?id=TbjEDwAAQBAJ

[9] J. A. W. M. H. W. P. E. LAGARIAS, J. C.; REEDS, "Convergence properties of the nelder–mead simplex method in low dimensions," *SIAM Journal on Optimization*, vol. 9, no. 1, pp. 112–147, 1998. [Online]. Available: https://doi.org/10.1137/S1052623496303470